Geophysical Research Letters

RESEARCH LETTER
10.1029/2020GL092251

Key Points:

- The wave component of boundary layer velocity profiles were measured in situ and decomposed by phase
- The wave velocity profile structure outside the boundary layer resembles that predicted by laminar theory
- Observations and modeling show a phase lag in eddy viscosity from boundary layer thickness and from dissipation

Correspondence to:
M. Cowherd,
cowherd@berkeley.edu

Citation:
Cowherd, M., Egan, G., Monismith, S., & Fringer, O. (2021). Phase-resolved wave boundary layer dynamics in a shallow estuary. *Geophysical Research Letters*, *48*, e2020GL092251. https://doi.org/10.1029/2020GL092251

Received 22 DEC 2020
Accepted 4 MAR 2021

Phase-Resolved Wave Boundary Layer Dynamics in a Shallow Estuary

Marianne Cowherd[1,2], Galen Egan[1], Stephen Monismith[1], and Oliver Fringer[1]

[1]Department of Civil and Environmental Engineering, Stanford University, Stanford, CA, USA, [2]Department of Environmental Science, Policy, and Management, University of California, Berkeley, Berkeley, CA, USA

Abstract We present in situ observations of near-bed velocity profiles with high temporal and spatial resolution from a Nortek Vectrino Profiler deployed in South San Francisco Bay. Using Hilbert analysis, we ensemble-averaged near-bed velocity profiles by wave phase and calculated wave phase-dependent boundary layer thickness for varying wave and current conditions. We also applied mixing length relationships to derive a boundary layer thickness-based eddy-viscosity and compared this estimate to one obtained from the k–ε turbulence model. From the eddy viscosity estimates, we find that while turbulence responds instantaneously to shear, boundary layer thickness lags by a scaling estimate based on the turbulence response timescale. This analysis provides a method for wave phase decomposition of field-based velocity profile time series and shows that there is a finite-time response between turbulence dissipation and boundary layer thickness.

Plain Language Summary We conducted field work in a muddy shoal of South San Francisco Bay to measure water velocity profiles within 2 cm of the bed. Motion in this region comes from waves and tidal currents; we present a new method for separating just the wave signal from a time series. We decompose the wave signal into bins determined by the instantaneous wave phase- and compare phase-binned profiles to predictions from theoretical models. For each of these phase-binned profiles, we calculate the size of the region in which the presence of the bed impacts flow characteristics. We investigate sources of discrepancy between observations and laminar theory, including turbulence and wave-roughness. Finally, we examine the relationship of these changing properties within the passage of a wave and describe the time it takes for the flow changes initiated by the wave to propagate upward. These results are important for understanding the contributions of waves to nearshore processes such as sediment transport and erosion.

1. Introduction

The thickness, δ, of an oscillatory laminar boundary layer generally scales as

$$\delta \sim \left(\frac{\nu}{\omega}\right)^{1/2}, \tag{1}$$

where ν is the kinematic viscosity and ω is the oscillation frequency (Nielsen, 1992). Applying this scaling to wind waves in estuaries, which often have periods of 2–3 s (Brand et al., 2010), gives a boundary layer thickness of $\mathcal{O}(10^{-3})$ m. Although a seemingly negligible fraction of the water column depth, the boundary layer plays an outsize role in determining sediment resuspension. Therefore, a comprehensive understanding of wave boundary layer dynamics is critical for accurately modeling sediment transport.

The laminar wave boundary layer was first described analytically by Stokes (1851), who derived the velocity profile $u(z, \theta)$ under an oscillating pressure gradient as

$$u(z,\theta) = u_b\left[\cos(\theta) - e^{-\frac{z}{\Delta}}\cos\left(\theta - \frac{z}{\Delta}\right)\right], \tag{2}$$

where u_b is the free-stream wave orbital velocity, θ is the phase, z is the height above the bed, and $\Delta = \left(\frac{2\nu}{\omega}\right)^{1/2}$ is the Stokes boundary layer thickness. However, because most environmental oscillatory flows are turbulent and sediment beds are typically rough, this idealized profile does not fully characterize behavior over a real bed with complex roughness elements.

Turbulent wave boundary layers over rough beds are modeled with semi-empirical theories that describe the nonlinear interaction between turbulence induced by waves and the mean flow in the bottom boundary layer (e.g., Christoffersen & Jonsson, 1985; Grant & Madsen, 1979). In general, these models predict that the mean flow feels greater bottom drag in the presence of waves and that turbulence acts to thicken the wave boundary layer according to the scaling

$$\delta \sim \frac{u_*}{\omega}, \tag{3}$$

where u_* is the friction velocity. In the Grant and Madsen (1979) model (hereafter GM), the resulting wave velocity takes the form

$$u(z,\theta) = \mathrm{Re}\left\{u_b e^{i\theta}\left[1 - \frac{\mathrm{ker}\left(2\zeta^{1/2}\right) + i\mathrm{kei}\left(2\zeta^{1/2}\right)}{\mathrm{ker}\left(2\zeta_0^{1/2}\right) + i\mathrm{kei}\left(2\zeta_0^{1/2}\right)}\right]\right\}, \tag{4}$$

where ker and kei are the zeroth-order Kelvin functions (Abramowitz & Stegun, 1970), $\zeta = zl^{-1}$ (with $l = \kappa u_* \omega^{-1}$), and $\zeta_0 = z_0 l^{-1}$, where z_0 is the bottom roughness and $\kappa = 0.41$ is the von Kármán constant. Due to the small scale of the wave boundary layer, it has most commonly been studied in laboratory settings. In the purely wave-driven case, turbulence measurements by Sleath (1987) indicated significant wave phase variability in turbulence statistics and eddy-viscosity, casting doubt on the applicability of the time-invariant eddy-viscosity assumed by many bottom boundary layer models (e.g., Grant & Madsen, 1979; You et al., 1991). Experiments with a mean flow indicated enhanced boundary layer turbulence in combined wave-current flows compared to pure current cases, with substantial variation over the wave cycle (Kemp & Simons, 1982). More recent studies have examined interactions between wave-driven turbulence and sediment in the bottom boundary layer, elucidating the roles of vortex generation over ripples (Nichols & Foster, 2007, 2009) and sediment-induced stratification (Hooshmand et al., 2015) in setting turbulence dynamics.

Though much has been learned from these laboratory studies, they do not represent field-scale combined wave-current forcing conditions. Foundational work by Foster et al. (2000) and Trowbridge and Agrawal (1995) reported two of the first sets of wave boundary layer field measurements. They found that many properties of Stokes theory held in the field, such as an increase in velocity amplitude and a decrease in phase with distance from the bed. Trowbridge and Agrawal (1995) also suggested that the wave boundary layer thickness increases with turbulence, supporting the dynamics assumed in GM. However, limitations in the measurement spatial resolution and temporal range along with complications arising from a shifting sediment bed reduced the generalizability of these studies. To date, the highest resolution field measurements of the combined wave-current boundary layer were presented by Nayak et al. (2015) using a custom submersible particle image velocimetry system. With a maximum spatial resolution of 4.2 mm, however, such a setup cannot resolve the wave boundary layer in shallow estuaries such as San Francisco Bay.

The Nortek Vectrino Profiler (Vectrino), an acoustic Doppler velocimeter (ADV) designed for laboratory use with 1 mm vertical resolution, presents an alternative to imaging-based boundary layer measurements (Craig et al., 2011). Using a field-adapted Vectrino, we measured combined wave-current boundary layer statistics with previously unmatched spatio-temporal resolution during a 16-day deployment in South San Francisco Bay. Because the Vectrino lacks a pressure sensor and internal clock shift precludes direct alignment between the Vectrino and an external pressure sensor, we propose a method for binning velocity measurements by wave phase by combining the Hilbert transform (Huang & Wu, 2008) with a spectral wave-turbulence decomposition (Bricker & Monismith, 2007). We present phase-averaged wave boundary

layer statistics for varying wave and tidal conditions and comment on the applicability of widely used models in describing boundary layer properties.

2. Methods

2.1. Field Data Collection

As part of a multi-season cohesive sediment transport and flocculation observation campaign, we deployed an instrumentation platform in South San Francisco Bay from 07/17/2018–08/15/2018 (see Egan, Cowherd, Fringer, & Monismith, 2019). Data are available at https://purl.stanford.edu/wv787xr0534 (Egan, Cowherd, Scheu, et al., 2019). At the study site, diurnal winds consistently drove waves toward the eastern shore each afternoon, and tidal currents of up to 30 cm s^{-1} ran primarily northwest-southeast along the major axis of the bay. Pressure measurements showed significant wave heights up to 50 cm during the deployment; wave bottom orbital velocities of up to 20 cm s^{-1} were calculated from Vectrino measurements.

The Vectrino was deployed at 37.58745°N, 122.18530°W with its measurement volume adjusted in situ by a diver to span 1 cm below to 2 cm above the bed (cmab), and logged all velocity components at a sampling frequency of 64 Hz for 12 min burst periods each hour. The vertical position of the Vectrino ensured that the expected boundary layer fell within the region with the highest signal-to-noise ratio (SNR; Koca et al., 2017; Thomas et al., 2017), and we selected the vertical range within the zone of high SNR for above-boundary layer vertical averages in the analysis. Previous work with data from this field campaign showed agreement between Vectrino velocity profiles and co-located ADV measurements above the Vectrino measurement volume (Egan et al., 2020), supporting the finding from Koca et al. (2017) that near-bed Vectrino measurements over soft beds align with validation measurements. We applied an algorithm from Thomas et al. (2017) to average Reynolds stress to account for changes in the SNR with height. We report velocity profiles from 0 to 1.5 cmab, as the platform sank 0.5 cm into the bed after deployment. Vectrino data were processed to remove spikes (Goring & Nikora, 2002) and rotated into the coordinate system defined by the dominant wave direction for each burst period, as determined by a co-located Nortek Vector ADV (Herbers et al., 1999).

2.2. Field Data Processing

In a combined wave-current flow, the horizontal velocity $u(z, t)$ measured by the Vectrino can be decomposed as

$$u(z,t) = \overline{u}(z) + \tilde{u}(z,t) + u'(z,t), \tag{5}$$

where $\overline{u}(z)$ is the time-averaged mean velocity, $\tilde{u}(z,t)$ is the wave-induced velocity, and $u'(z, t)$ is the turbulent contribution. In order to isolate the wave velocity, we modified the method described by Bricker and Monismith (2007), which is used to decompose wave and turbulence-driven momentum fluxes. First, we vertically averaged the Vectrino profile from 1.0 to 1.5 cmab (within the high SNR range) and detrended the resulting time series to obtain a representative fluctuating velocity, $u_p(t) = \tilde{u}_p(t) + u_p'(t)$, which is assumed to be the potential flow region above the wave boundary layer. We then extracted the purely wave-induced power spectrum, $S_{\tilde{u}\tilde{u}}$, from u_p. This was accomplished by linearly interpolating the full power spectrum, S_{uu}, under its wave peak in log-space, and subtracting the interpolated portion, $\hat{S}_{uu}$, from the full spectrum. The wave frequency range generally spanned from $0.4f_{max}$ to $1.4f_{max}$, where f_{max} is the frequency corresponding to the maximum power spectral density. Assuming that $\hat{S}_{uu}$ is representative of the turbulence power spectrum in the wave range, the portion of the spectrum due solely to waves is then

$$S_{\tilde{u}\tilde{u}} = S_{uu} - \hat{S}_{uu}. \tag{6}$$

We identified burst periods that contained sufficient waves for a wave decomposition as bursts in which the peak value of $S_{\tilde{u}\tilde{u}}$ was greater than the 90th-percentile value of $S_{uu} - \hat{S}_{uu}$ outside of the wave frequency range. This criterion compares a tentatively identified wave signal to the turbulence seen at all frequencies; only bursts with wave signals that satisfy the criterion were analyzed for wave phase decomposition.

From the wave power spectrum $S_{\tilde{u}\tilde{u}}$ we constructed the real Fourier series amplitudes within the wave range as

$$\tilde{A} = \sqrt{S_{\tilde{u}\tilde{u}} d\omega}, \tag{7}$$

where $d\omega$ is the radian frequency resolution. We next set $\tilde{A} = 0$ outside of the wave frequency range, and computed the inverse Fourier transform to recover the wave velocity in the potential flow region,

$$\tilde{u}_p(t) = \mathcal{F}^{-1}\left(\tilde{A}e^{i\phi}\right), \tag{8}$$

where the phase, ϕ, of the original signal is assumed to be solely influenced by waves. The resulting time series $\tilde{u}_p$ is a reasonable reconstruction of the wave contribution over the measurement period in the absence of significant wave-turbulence interactions.

Next, we identify the instantaneous phase associated with each measurement in the wave velocity time series. This is accomplished by first applying the Hilbert transform to $\tilde{u}_p$, resulting in the analytic signal

$$Z(t) = \tilde{u}_p + i\mathcal{H}(\tilde{u}_p), \tag{9}$$

where $\mathcal{H}$ is the Hilbert transform. We then compute the instantaneous phase $\theta(t)$ as

$$\theta(t) = \arctan\left(\frac{\mathcal{H}(\tilde{u}_p)}{\tilde{u}_p}\right) = \arctan\left(\frac{\mathrm{Im}(Z)}{\mathrm{Re}(Z)}\right). \tag{10}$$

We then return to the raw Vectrino data, binning each instantaneous profile by phase and averaging the total fluctuating velocity, $u(z,t) - \overline{u}(z) = \tilde{u}(z,t) + u'(z,t)$, within each bin to obtain phase-averaged velocity profiles, denoted $u(z, \theta)$. The choice of eight phase bins of size $\pi/4$ each provided representative demonstration of between-phase variations while retaining statistical confidence from large sample sizes per bin ($N = 5{,}000$ per bin per burst). Each burst had 46,080 records in time, giving >5,000 samples per phase bin per burst. This analysis gave velocity profiles $u(z, \theta)$ for each burst which could then be normalized by representative wave orbital velocities u_b were defined as the root-mean-square of $\tilde{u}_p(t)$ for each burst.

Previous studies have presented multiple definitions for the wave boundary layer thickness. These include the location below the overshoot region where the local velocity equals the free-stream velocity (Jonsson, 1980), the location where the velocity equals 95% of the free-stream velocity (Sleath, 1987), and the zero-crossing location of the Reynolds stress (Hooshmand et al., 2015). Each of these methods provided noisy boundary layer thickness estimates for our data, so we instead propose an integral-based method derived from a modified definition for the boundary layer displacement thickness (Schlichting & Gersten, 2016). First, we consider the vertical Vectrino range from 0 to 1 cmab. This vertical limitation removed measurements with a poor SNR, and based on visual inspection of the profiles, retained the region containing the boundary layer. The phase-varying thickness of the boundary layer was then calculated as

$$\delta(\theta) = \alpha \int_0^{z_m} \left(1 - \frac{|\, u(z,\theta)\,|}{\max\left(|\, u(z,\theta)\,|\right)}\right) \mathrm{d}z \tag{11}$$

where z_m is the vertical coordinate of the maximum absolute value of the velocity profile, and α is a constant of proportionality. For steady wall-bounded flows, $\alpha \approx 3$ relates the displacement thickness to the boundary layer thickness (Schlichting & Gersten, 2016). For oscillatory boundary layers, there is no obvious choice for α, but based on the results shown in Figure 1, we find that $\alpha = 2$ provides a reasonable estimate of the boundary layer thickness.

There are several relevant methods for calculating the friction velocity u_*. In this analysis, we use both GM and a combined wave-current friction velocity derived from our measurements as described in Egan, Cowherd, Fringer, and Monismith (2019). We also calculated phase-decomposed turbulence kinetic energy (TKE) from the wave-turbulence decomposed velocity measurements with

$$k(z,\theta) = \frac{1}{2}\left(\overline{u'(z,\theta)^2} + \overline{v'(z,\theta)^2} + \overline{w'(z,\theta)^2}\right) \tag{12}$$

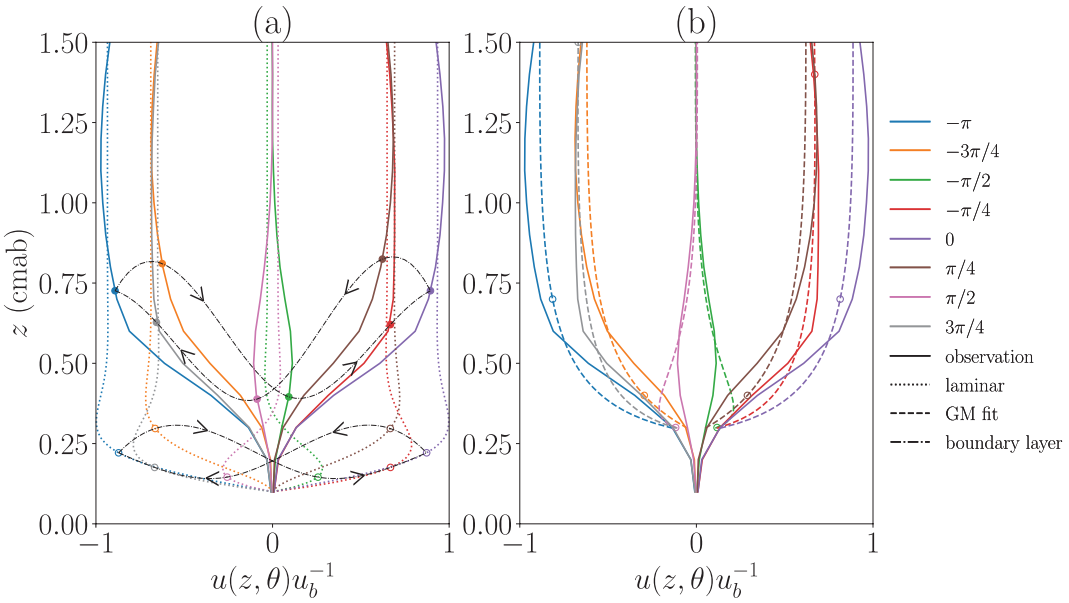

Figure 1. Observed velocity profiles over the first 1.5 cm above the bed (solid lines), with individual wave phases indicated by color. Profiles from all 323 wavy bursts are normalized by the wave orbital velocity u_b before ensemble averaging. Panel (a) shows corresponding phase-averaged laminar solutions (Equation 2, dotted lines) for representative wave conditions. Dots indicate boundary layer height at each phase; boundary layer height at intermediate phases fall along the connecting dash-dotted line with arrows indicating forward-in-time wave propagation. Panel (b) shows the best-fit of Equation 4 to phase-binned profiles.

where the overbar represents the ensemble average in each phase bin. Following Feddersen et al. (2007), we also calculated the burst-averaged TKE dissipation rate, $\langle\varepsilon(z)\rangle$. Because the dissipation rate estimation method relied on spectral curve fitting, we could not directly estimate phase-averaged $\varepsilon(z,\theta)$. Such an estimate could be made for Vectrino Profiler data using a structure function approach (Pope, 2001). However, structure function-based dissipation estimates proved inconsistent with multiple spectral methods (Feddersen et al., 2007; Trowbridge & Elgar, 2001). The bottom wave orbital velocity u_b was estimated as the root-mean-square of the fluctuating horizontal velocity, $u_p(t)$, in the top five Vectrino bins, as described in Egan, Cowherd, Fringer, and Monismith (2019).

To characterize the structure of the phase-binned velocity profiles, we fit them to the GM solution (Equation 4), optimizing to find a best-fit u_*. However, this procedure required a modification because the near-bed mean flow at the study site was well-parameterized by a canopy flow model (Egan, Cowherd, Fringer, & Monismith, 2019), rather than the logarithmic layer assumed by GM. This resulted in negative curvature of the profiles in the canopy region and a velocity zero-crossing at $z = d$ rather than $z = 0$, where d is the canopy displacement parameter (Ghisalberti & Nepf, 2009). Therefore, we adjusted the vertical coordinate by an offset $d = 0.25$ cm and carried out the regression using data in the range 0.4–1.2 cmab (the region where the velocity profile was logarithmic). The value of d was selected to optimize the model fit to the observations and is consistent with observations of the bed structures. After regressing for u_* and assuming a linear eddy-viscosity profile, we estimated a velocity profile-based eddy-viscosity

$$\nu_*(z) = \kappa u_* z. \tag{13}$$

While GM assumes a constant eddy-viscosity profile in time, we allowed u_* to vary with wave phase. In addition to the regression-based and phase-varying u_* in Equation 13, we will report values of u_{*m}, the phase-invariant, combined wave-current friction velocity measured by the Vectrino. Full details of that calculation can be found in Egan, Cowherd, Fringer, and Monismith (2019), but in brief, it is estimated from the sum of the near-bed turbulent Reynolds stress, wave momentum flux, and viscous stress.

2.3. Numerical Modeling

In order to compare measured turbulence statistics to those derived from a common modeling framework, we simulated a combined wave-current boundary layer using the General Ocean Turbulence Model (GOTM; Burchard et al., 1999). Though GOTM was not originally developed to examine high-frequency (i.e., on the timescale of estuarine wind waves) boundary layer processes, its two-equation turbulence closures do, in principle, allow for the calculation of wave phase-resolved turbulence statistics. This is a more advanced treatment than GM, which was formulated as a phase-averaged model, and therefore should be adequate for examining the interplay between TKE dissipation and boundary layer growth.

We discretized a 2.5 m water column into 100 vertical bins with a bottom-zooming factor $d_l = 4$ (Umlauf et al., 2006), which stretches the grid to give a minimum grid spacing of $\Delta z = 0.15$ mm at the bed. The flow was forced with a steady pressure gradient corresponding to $u_* = 0.01$ m s^{-1}, typical of the field conditions. After spinning the model up to steady state, an oscillating pressure gradient with period $T = 3$ s and free surface deflection amplitude $\eta = 0.1$ m was superimposed on the steady current. The physical (Nikuradse) bottom roughness was set to $k_b = 1$ cm, consistent with previous work examining bottom drag at the study site (Egan et al., 2020). We chose a k–ε model for the turbulence closure because its form of the eddy-viscosity,

$$\nu_{k\langle\varepsilon\rangle} = C_\mu \frac{k^2}{\langle\varepsilon\rangle}, \tag{14}$$

where $C_\mu = 0.09$ is an empirical constant, can also be evaluated using measured data. Additionally, the model results provide phase-varying dissipation rate estimates, allowing for a comparison between $\nu_{k\langle\varepsilon\rangle}$ defined in Equation 14 and an analogous $\nu_{k\varepsilon}$ using $\varepsilon(\theta)$ rather than $\langle\varepsilon\rangle$. After running the simulation for 500 wave periods, modeled turbulence statistics were binned by wave phase following the same procedure as the field measurements (Section 2.2).

3. Results

3.1. Phase-Decomposed Velocity

All bursts showed similar phase variability in the velocity profiles $u(z, \theta)$. However, in order to produce smooth profiles for comparison to the theory, we first normalized the profiles by the wave orbital velocity for each burst u_b and then ensemble-averaged the normalized profiles over the bursts in the record that had a sufficient wave signal (323 of the 384 bursts during the 16-day deployment). The peak wave frequency for these bursts varied from 0.26 to 0.54 Hz, with an average of 0.34 Hz throughout the deployment duration. Figure 1a shows the normalized and ensemble-averaged profiles with the boundary layer thickness indicated for each phase. The dash-dotted line in Figure 1a indicates the progression of the boundary layer thickness throughout the wave cycle. Above the boundary layer, observations track the velocity magnitude and structure of the laminar solution. This indicates that potential flow theory accurately captures the phase-varying flow kinematics further from the bed, and that deviations from theory, especially in the enhanced boundary layer thickness, arise from turbulence and roughness.

In Figure 1b, best-fit profiles of the GM solution (Equation 4) show agreement with observations, with an average residual of 9.3%, with the highest error at phases $\theta = \pm\,\pi/2$ and lowest at $\theta = 0, -\pi$. Above the boundary layer height, the average residual for all phases is 7.6%. The best-fit to Equation 4 shown in Figure 1b is significantly better than the laminar solution in Figure 1a, which reflects the fact that Equation 4 accounts for a turbulent combined wave-current flow. Still, neither model captures the negative curvature of the velocity profiles in the canopy region. The best-fit u_* values and resulting turbulent eddy-viscosity profiles at each phase are discussed in Section 3.3.

3.2. Boundary Layer Thickness

Dots on both the observed profiles and laminar solutions in Figure 1a indicate the boundary layer thickness defined by Equation 11. There is significant boundary layer thickening in the observations compared to

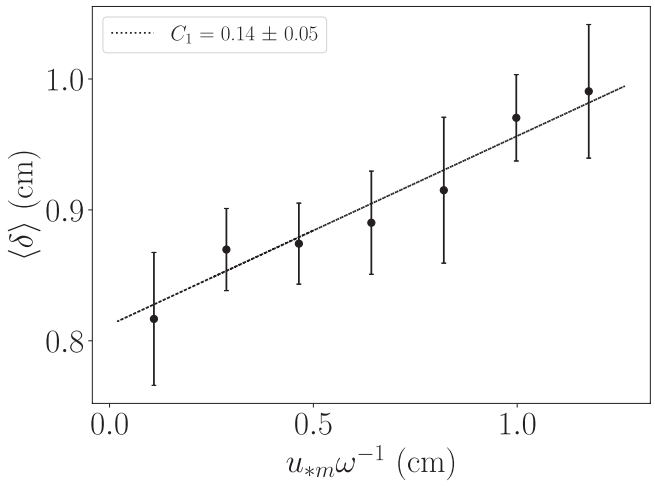

Figure 2. Burst-representative boundary layer thickness $\langle\delta\rangle$ as a function of $u_{*m}\omega^{-1}$, with the slope of the best-fit linear regression given by C_1. The error bound on C_1 is a bootstrapped 95% confidence interval.

the corresponding phase of the laminar solution. The observed boundary layer is 82.8% thicker than that in the laminar solution across all wave phases.

To compare boundary layer thickness between measurement bursts with different wave conditions, we define a burst-representative boundary layer thickness $\langle\delta\rangle$ as the average of values at $\theta = 3\pi/2$ and $\theta = \pi/4$ for each burst. These phases have the highest values of $\delta(\theta)$ for all bursts and are therefore the most applicable to models based on maximum wave orbital velocity, such as GM. The phases at which $\delta(\theta)$ are maximized lag behind the phases at which the wave-oriented velocity are maximized, which is discussed further below. As expected from Equation 3, the boundary layer thickness varied linearly with $u_{*m}\omega^{-1}$ with a slope C_1 (Figure 2). The slope $C_1 = 0.14 \pm 0.05$ estimated from our data is similar to previously reported scaling relationships, for example, $C_1 = 0.15$ (Christoffersen & Jonsson, 1985), $C_1 = 0.2$ (You et al., 1992), and $C_1 = 0.36$ (Hsu & Jan 1998), and significantly smaller than others, for example, $C_1 = 0.8$ (Grant & Madsen, 1979).

3.3. Turbulent Eddy-Viscosity

As described in Section 2.2, we estimated the turbulent eddy-viscosity through multiple methods. The first estimate, ν_*, is based on Equation 13 after fitting the GM solution (Equation 4) to the phase-varying velocity profiles. An independent estimate of the eddy-viscosity is based on the k–ε model (Equation 14), where eddy-viscosity values are vertically averaged from 0.4 to 1.2 cmab (identical to the GM velocity profile regression region). Finally, we can define a representative eddy-viscosity based on the boundary layer thickness. Combining a mixing length relationship $\nu_\delta = \kappa u_* \delta$ with the results in Figure 2, that is, $\delta = C_1 u_* \omega^{-1}$, we obtain

$$\nu_\delta = \frac{\kappa}{C_1}\delta^2\omega. \tag{15}$$

Up to the constant factor C_1, this estimate is based solely on the boundary layer thickness derived from measured velocity profiles (Equation 11) and the wave frequency. A comparison of the three eddy-viscosity estimates based on the measurements is shown in Figure 3a, where the eddy viscosity estimates at each measurement burst period are first nondimensionalized by $\kappa u_{*m} z$, and then ensemble-averaged across the deployment period for each wave phase.

Of the eddy-viscosity estimates in Figure 3a, ν_δ and $\nu_{k\langle\varepsilon\rangle}$ are similar in terms of magnitude, suggesting that (a) the k–ε model can accurately capture the interplay between turbulent dissipation and boundary layer growth, and (b) the relatively simple scalings in Figure 2 and Equation 15 are representative of the turbulence dynamics. While the factor $C_1 = 0.14$ appears to be appropriate when comparing ν_δ to $\nu_{k\langle\varepsilon\rangle}$, setting $C_1 = 1.7$ would result in better agreement between ν_δ and ν_*, as the profile-based ν_* is significantly smaller than either of the other two estimates. This discrepancy could be due to the canopy dynamics that GM does not resolve. While ν_δ and $\nu_{k\langle\varepsilon\rangle}$ are based on direct measurements of the boundary layer thickness and turbulence statistics, respectively, ν_* relies on implicit assumptions about the near-bed flow structure which do not hold over a canopy-like bed, potentially resulting in an underestimation of the eddy-viscosity. This result speaks to the importance of high-resolution, near-bed flow measurements, which can reveal unexpected dynamics that fall outside the range of common modeling assumptions.

Though the magnitudes of ν_δ and $\nu_{k\langle\varepsilon\rangle}$ are similar, they are phase-shifted from each other, with the peak in ν_δ lagging the peak in $\nu_{k\varepsilon}$. The velocity profile-based eddy-viscosity, ν_*, is approximately in phase with $\nu_{k\langle\varepsilon\rangle}$, indicating that both estimates respond instantaneously to the maximum wave velocity (Figure 1). This contrasts with ν_δ, which peaks with the maximum boundary layer thickness. The boundary layer growth timescale can be calculated as an optimal lag that maximizes the correlation between $\nu_{k\varepsilon}$ and ν_δ. That lag is consistent with $\langle C_\mu k \langle\varepsilon\rangle^{-1}\rangle$, a scaling estimate for the turbulence response or decay time (averaged across all

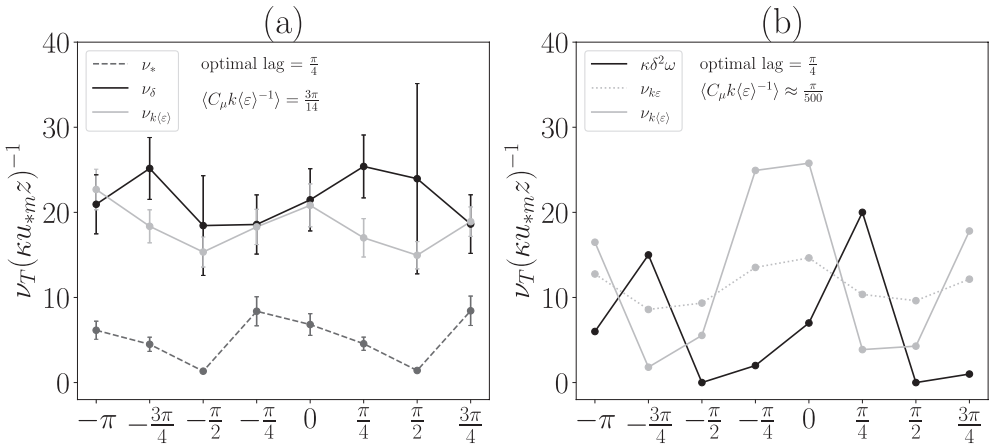

Figure 3. Comparison of the eddy-viscosity estimated via boundary layer thickness scaling (ν_δ, black markers) and k–ε model ($\nu_{k\langle\varepsilon\rangle}$, gray markers). Panel (a) shows measured data, including the velocity profile-based eddy-viscosity ν_* (gray dashed line). $k^2\langle\varepsilon\rangle^{-1}$ is averaged from 0.4 to 1.2 cmab and the constant of proportionality $C_1 = 0.14$ is derived from the best-fit slope in Figure 2. Panel (b) shows GOTM-derived data with $k^2\langle\varepsilon\rangle^{-1}$ evaluated at $z = 0$, and includes $\nu_{k\varepsilon}$ evaluated using instantaneous dissipation rate data (gray dotted line) for comparison. All eddy viscosity estimates are nondimensionalized by $\kappa u_{*m} z$ prior to ensemble averaging. The time lag (in wave phase units) that maximizes the lagged correlation between ν_δ and $\nu_{k\langle\varepsilon\rangle}$ is also indicated, along with the turbulence decay timescale $\langle C_\mu k\langle\varepsilon\rangle^{-1}\rangle$.

wave phases). This agreement indicates that the boundary layer thickness adjusts to turbulent dissipation in the boundary layer at approximately the expected turbulence timescale. The optimal lag is also identical to the phase lag between the maximum phase-averaged velocity and maximum boundary layer thickness (Figure 1a).

A similar analysis can be carried out using the GOTM results, as shown in Figure 3b. Unlike in the measured data, however, the modeled eddy-viscosity only showed significant wave phase variability in the grid cells closest to the bed, contrasting with the strong variability up to 1 cmab in the measurements. Therefore, the k–ε estimate in Figure 3b is taken from the bottom-most model grid cell. This resulted in a smaller k–ε eddy-viscosity when compared to the measurements. The results in Figure 3b also validate the assumption that $\langle\varepsilon\rangle$ is an adequate replacement for $\varepsilon(\theta)$ when calculating $\nu_{k\langle\varepsilon\rangle}$. Although the magnitude of $\nu_{k\langle\varepsilon\rangle}$ varies more widely over the wave period than $\nu_{k\varepsilon}$, the two estimates produce similar mean values and are in phase with each other.

One significant difference between the modeled and measured data is that the boundary layer thickness-based estimate in Figure 3b did not require a scaling factor in order to approximately match the k–ε estimate. The phase lag behavior, in terms of the optimal lag between ν_δ and $\nu_{k\varepsilon}$, was similar to the measured data. The modeled optimal lag, however, was greater than the modeled turbulence timescale (using the values of k and $\langle\varepsilon\rangle$ in the bottom grid cell) by over two orders of magnitude. Using k and $\langle\varepsilon\rangle$ vertically averaged between 0.4 and 1.2 cmab (as in Figure 3a) resulted in $\left\langle C_\mu k\left\langle\varepsilon\right\rangle^{-1}\right\rangle \approx \frac{\pi}{100}$. Examining k and ε individually, the mismatch between the measured and modeled turbulence timescale is primarily due to the modeled near-bed dissipation exceeding the measured dissipation by approximately two orders of magnitude (not shown). That discrepancy, combined with the lack of wave phase variability in turbulence statistics outside ≈0.2 cmab suggests that a one-dimensional k–ε closure with law-of-the-wall boundary conditions cannot represent the nuanced bottom boundary layer dynamics in a combined wave-current flow over a rough bed.

The flow kinematics (i.e., the velocity profiles used to estimate the boundary layer thickness) were more consistent between the model and measurements than the turbulence statistics. Nevertheless, the model underestimated the boundary layer thickness at the two maximum phases by an average factor of 1.7. This disparity could be due partially to the heterogeneous bed geometry at our study site, which induced strong wave momentum fluxes (i.e., $\overline{\tilde{u}\tilde{w}}$ as discussed in Egan, Cowherd, Fringer, & Monismith, 2019). The GOTM implementation did not include these complexities, nor any second-order nonlinearities (e.g., terms like

$u\frac{\partial u}{\partial x}$), which lead to effects such as boundary layer streaming over smooth beds (Longuet-Higgins, 1953). Overall though, the agreement in phase relationship between the near-bed eddy-viscosity and boundary layer thickness in both the model and the measurements indicates that these dynamics are likely consistent across a range of combined wave-current boundary layer flows.

4. Conclusions

We presented a signal processing-based wave phase decomposition of field observations from a single profiling velocimeter, allowing us to observe phase-varying flow properties within a wave-current boundary layer. This method diminishes the potential for errors resulting from clock drift between a velocimeter and a separate pressure logger. The Hilbert transform is an effective method for decomposing high-frequency velocity profiles by wave phase and shows that instantaneous wave-induced velocities significantly diverge from the time-averaged near-bed flow. At our study site in South San Francisco Bay, the magnitude of wave contributions to the flow velocity within the boundary layer was similar to the contribution from tidal currents. While time-averaged flow properties can characterize bed processes that occur over tidal or seasonal timescales, ensemble averaging over wave phase is essential for understanding the significant variations on the timescale of waves.

From the phase-varying velocity profiles, we proposed a novel estimate for the boundary layer thickness based on the displacement thickness (Equation 11). Though our choice of $\alpha = 2$ was arbitrary, it produced reasonable results despite the inherent noise in the field observations. Furthermore, the eddy-viscosity constructed using the boundary layer thickness (Equation 15) was consistent in magnitude with an estimate based on a k–ε turbulence model (Equation 14). This further justifies our choice of $\alpha = 2$ and suggests that a simple scaling estimate based on mixing length arguments can adequately describe near-bed wave-current turbulence dynamics.

We also demonstrated the applicability of the GM oscillatory flow solution to our measured velocity profiles outside the canopy region. This agreement did not extend to the eddy-viscosity, which our measurements indicate was enhanced by interactions between the turbulent flow and the canopy elements. Additionally, by allowing the slope of the eddy-viscosity profile to vary with wave phase, we showed that the turbulent eddy-viscosity changes in time under wavy conditions. Given the significance of waves on the velocity profile structure, this is a physically reasonable expectation of real flows.

One of the most striking results from this work was the existence of a phase lag between ν_δ and $\nu_{k\langle\varepsilon\rangle}$. Further, there is agreement between the expected turbulence timescale and the optimal phase lag between ν_δ and $\nu_{k\langle\varepsilon\rangle}$. While $\nu_{k\langle\varepsilon\rangle}$ is in phase with the instantaneous wave velocity and vertical shear, ν_δ lags behind as momentum is transported away from the boundary by turbulent diffusion. This lag is confirmed by both observations and numerical modeling and indicates that the boundary layer thickness responds to turbulent mixing in a finite amount of time. Previous analytical work has assumed a constant boundary layer thickness based on a time-invariant shear stress (e.g., GM) or assumed instantaneous boundary layer response to shear stress. However, by analyzing field measurements with fine spatial and temporal resolution, we show that real wave-current boundary layer behavior deviates from these assumptions.

Though our analysis focused solely on hydrodynamics, the results have obvious implications for sediment transport. The results in Figure 3 indicate that the turbulent eddy-viscosity can vary by approximately a factor of two over the wave cycle. Such an increase could lead to enhanced erosion during certain wave phases that would not necessarily be captured by wave-averaged parameterizations. In general, wave-averaged estimations may underestimate sediment transport because they do not resolve phases where the critical shear stress for erosion is exceeded, despite the mean shear stress falling below the threshold. Future work should focus on quantifying the phase-varying nature of sediment resuspension and the potential impacts on associated parameterizations in coarser, time-averaged models.

Conflict of Interest

The authors declare no conflicts of interest.

Data Availability Statement

The data used in this study are available under a Creative Commons Attribution-Noncommercial-Share Alike 3.0 Unported License through the Stanford Digital Repository at https://purl.stanford.edu/wv787xr0534 (Egan, Cowherd, Scheu, et al., 2019). Code used in this study can be accessed online at https://github.com/mariannecowherd/efml.

Acknowledgments
M. C. gratefully acknowledges the support of the Stanford Vice Provost for Undergraduate Education and G. E. acknowledges the support of the Charles H. Leavell Graduate Fellowship. This work was funded by the U.S. National Science Foundation under Grant OCE-1736668. The authors thank Frank Spada, Kara Scheu, Grace Chang, Craig Jones, Sam McWilliams, Stephen LaMothe, and Jim Christmann for their assistance with the field work. The authors also thank the two anonymous reviewers, whose suggestions improved the quality of this manuscript.

References

Abramowitz, M., & Stegun, I. A. (1970). Handbook of Mathematical Functions With Formulas, Graphs, and Mathematical Tables (Vol. 55). US Government printing office.

Brand, A., Lacy, J. R., Hsu, K., Hoover, D., Gladding, S., & Stacey, M. T. (2010). Wind-enhanced resuspension in the shallow waters of South San Francisco Bay: Mechanisms and potential implications for cohesive sediment transport. *Journal of Geophysical Research*, *115*(C11). https://doi.org/10.1029/2010jc006172

Bricker, J. D., & Monismith, S. G. (2007). Spectral wave-turbulence decomposition. *Journal of Atmospheric and Oceanic Technology*, *24*(8), 1479–1487. https://doi.org/10.1175/jtech2066.1

Burchard, H., Bolding, K., & Villarreal, M. (1999). *GOTM, a general ocean turbulence model: Scientific documentation* (Technical Report). Ispra: European Community.

Christoffersen, J. B., & Jonsson, I. G. (1985). Bed friction and dissipation in a combined current and wave motion. *Ocean Engineering*, *12*(5), 387–423. https://doi.org/10.1016/0029-8018(85)90002-2

Craig, R. G., Loadman, C., Clement, B., Rusello, P. J., & Siegel, E. (2011). Characterization and testing of a new bistatic profiling acoustic Doppler velocimeter: The Vectrino-II. In *2011 IEEE/OES 10th Current, Waves and Turbulence Measurements (CWTM)* (pp. 246–252).

Egan, G., Chang, G., Revelas, G., Monismith, S., & Fringer, O. (2020). Bottom drag varies seasonally with biological roughness. *Geophysical Research Letters*, *47*, e2020GL088425. https://doi.org/10.1029/2020gl088425

Egan, G., Cowherd, M., Fringer, O., & Monismith, S. (2019). Observations of near-bed shear stress in a shallow, wave- and current-driven flow. *Journal of Geophysical Research: Oceans*, *124*, 6323–6344. https://doi.org/10.1029/2019jc015165

Egan, G., Cowherd, M., Scheu, K., Spada, F., Manning, A., Jones, C., et al. (2019). *South San Francisco Bay boundary layer and sediment dynamics field data*. Stanford Digital Repository. Retrieved from https://purl.stanford.edu/wv787xr0534

Feddersen, F., Trowbridge, J. H., & Williams, A. J., III (2007). Vertical structure of dissipation in the nearshore. *Journal of Physical Oceanography*, *37*(7), 1764–1777. https://doi.org/10.1175/jpo3098.1

Foster, D. L., Beach, R. A., & Holman, R. A. (2000). Field observations of the wave bottom boundary layer. *Journal of Geophysical Research*, *105*(C8), 19631–19647. https://doi.org/10.1029/1999jc900018

Ghisalberti, M., & Nepf, H. (2009). Shallow flows over a permeable medium: The hydrodynamics of submerged aquatic canopies. *Transport in Porous Media*, *78*(2), 309. https://doi.org/10.1007/s11242-008-9305-x

Goring, D. G., & Nikora, V. I. (2002). Despiking acoustic Doppler velocimeter data. *Journal of Hydraulic Engineering*, *128*(1), 117–126. https://doi.org/10.1061/(asce)0733-9429(2002)128:1(117)

Grant, W. D., & Madsen, O. S. (1979). Combined wave and current interaction with a rough bottom. *Journal of Geophysical Research*, *84*(C4), 1797–1808. https://doi.org/10.1029/jc084ic04p01797

Herbers, T. H. C., Elgar, S., & Guza, R. T. (1999). Directional spreading of waves in the nearshore. *Journal of Geophysical Research*, *104*(C4), 7683–7693. https://doi.org/10.1029/1998jc900092

Hooshmand, A., Horner-Devine, A. R., & Lamb, M. P. (2015). Structure of turbulence and sediment stratification in wave-supported mud layers. *Journal of Geophysical Research: Oceans*, *120*, 2430–2448. https://doi.org/10.1002/2014jc010231

Hsu, T.-W., & Jan, C.-D. (1998). Calibration of Businger-Arya type of Eddy viscosity model's parameters. *Journal of Waterway, Port, Coastal, and Ocean Engineering*, *124*(5), 281–284. https://doi.org/10.1061/(asce)0733-950x(1998)124:5(281)

Huang, N. E., & Wu, Z. (2008). A review on Hilbert-Huang transform: Method and its applications to geophysical studies. *Reviews of Geophysics*, *46*(2). https://doi.org/10.1029/2007rg000228

Jonsson, I. G. (1980). A new approach to oscillatory rough turbulent boundary layers. *Ocean Engineering*, *7*(1), 109–152. https://doi.org/10.1016/0029-8018(80)90034-7

Kemp, P. H., & Simons, R. R. (1982). The interaction between waves and a turbulent current: Waves propagating with the current. *Journal of Fluid Mechanics*, *116*, 227–250. https://doi.org/10.1017/s0022112082000445

Koca, K., Noss, C., Anlanger, C., Brand, A., & Lorke, A. (2017). Performance of the Vectrino profiler at the sediment-water interface. *Journal of Hydraulic Research*, *55*(4), 573–581. https://doi.org/10.1080/00221686.2016.1275049

Longuet-Higgins, M. S. (1953). Mass transport in water waves. *Philosophical Transactions of the Royal Society of London – Series A: Mathematical and Physical Sciences*, *245*(903), 535–581.

Nayak, A. R., Li, C., Kiani, B. T., & Katz, J. (2015). On the wave and current interaction with a rippled seabed in the coastal ocean bottom boundary layer. *Journal of Geophysical Research: Oceans*, *120*, 4595–4624. https://doi.org/10.1002/2014jc010606

Nichols, C., & Foster, D. (2007). Full-scale observations of wave-induced vortex generation over a rippled bed. *Journal of Geophysical Research*, *112*(C10). https://doi.org/10.1029/2006jc003841

Nichols, C., & Foster, D. (2009). Observations of bed form evolution with field-scale oscillatory hydrodynamic forcing. *Journal of Geophysical Research*, *114*(C8). https://doi.org/10.1029/2008jc004733

Nielsen, P. (1992). Coastal bottom boundary layers and sediment transport (Vol. 4). World scientific.

Pope, S. B. (2001). *Turbulent flows*. IOP Publishing.

Schlichting, H., & Gersten, K. (2016). *Boundary-layer theory*. Springer.

Sleath, J. F. A. (1987). Turbulent oscillatory flow over rough beds. *Journal of Fluid Mechanics*, *182*, 369–409. https://doi.org/10.1017/s0022112087002374

Stokes, G. G. (1851). On the Effect of the Internal Friction of Fluids on the Motion of Pendulums (Vol. 9). Pitt Press.

Thomas, R., Schindfessel, L., McLelland, S., Creëlle, S., & De Mulder, T. (2017). Bias in mean velocities and noise in variances and covariances measured using a multistatic acoustic profiler: The Nortek Vectrino Profiler. *Measurement Science and Technology*, *28*(7), 075302. https://doi.org/10.1088/1361-6501/aa7273

Trowbridge, J., & Elgar, S. (2001). Turbulence measurements in the surf zone*. *Journal of Physical Oceanography*, *31*(8), 2403–2417. https://doi.org/10.1175/1520-0485(2001)031<2403:tmitsz>2.0.co;2

Trowbridge, J. H., & Agrawal, Y. C. (1995). Glimpses of a wave boundary layer. *Journal of Geophysical Research*, *100*(C10), 20729–20743. https://doi.org/10.1029/95jc02131

Umlauf, L., Burchard, H., & Bolding, K. (2006). *GOTM: Source code and test case documentation, Devel version-pre, 4*. Retreived from https://gotm.net/manual/stable/pdf/a4.pdf

You, Z.-J., Wilkinson, D., & Nielsen, P. (1991). Velocity distributions of waves and currents in the combined flow. *Coastal Engineering*, *15*(5–6), 525–543. https://doi.org/10.1016/0378-3839(91)90026-d

You, Z.-J., Wilkinson, D., & Nielsen, P. (1992). Velocity distribution in turbulent oscillatory boundary layer. *Coastal Engineering*, *18*(1–2), 21–38. https://doi.org/10.1016/0378-3839(92)90003-d